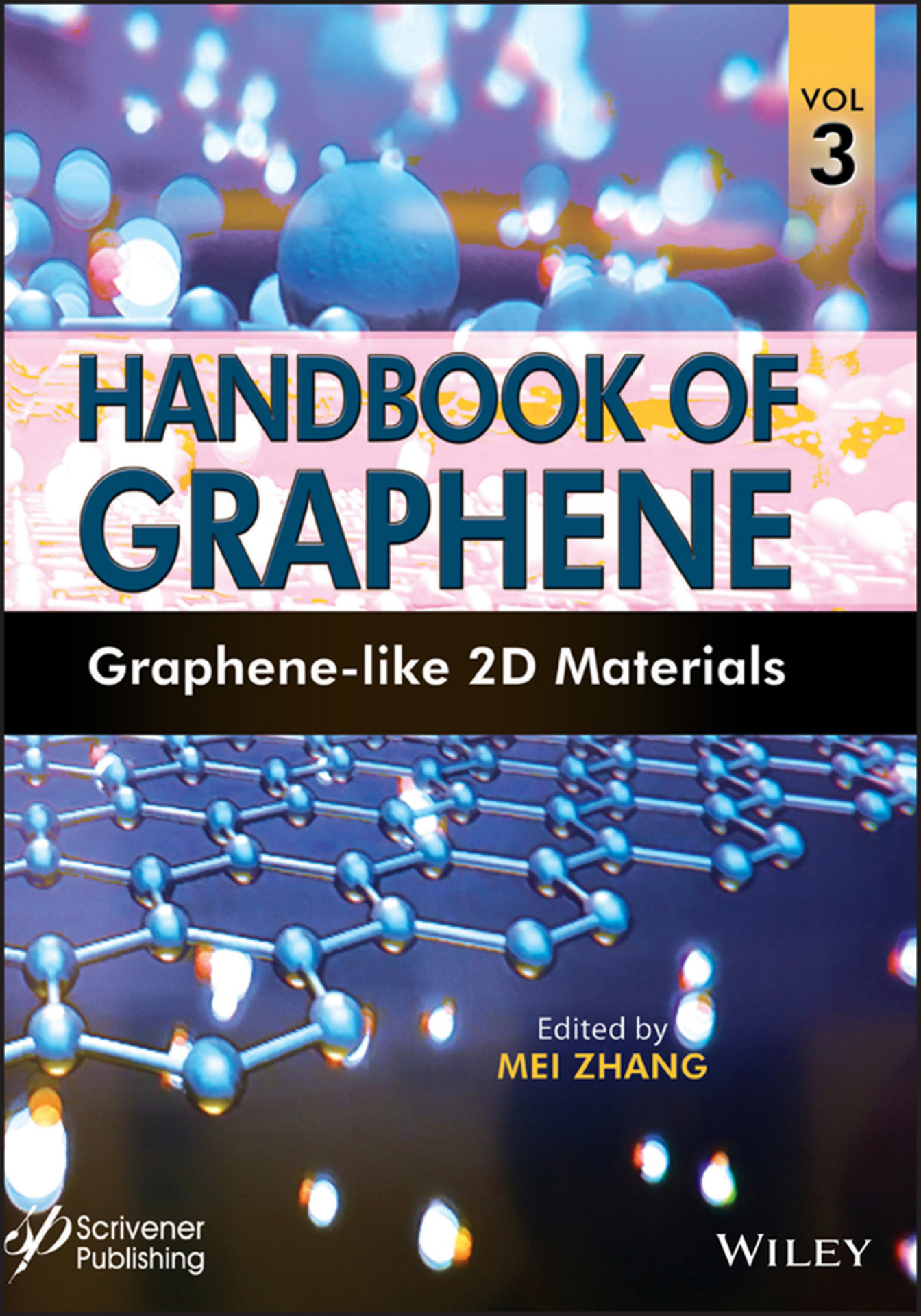
VOL
3
HANDBOOK OF
GRAPHENE
Graphene-like 2D Materials
Edited by
MEI ZHANG
Scrivener
Publishing
WILEY

Handbook of Graphene

Scrivener Publishing
100 Cummings Center, Suite 541J
Beverly, MA 01915-6106

Publishers at Scrivener
Martin Scrivener (martin@scrivenerpublishing.com)
Phillip Carmical (pcarmical@scrivenerpublishing.com)

Handbook of Graphene comprises 8 volumes:

Volume 1: Growth, Synthesis, and Functionalization
Edited by Edvige Celasco and Alexander Chaika
ISBN 978-1-119-46855-4

Volume 2: Physics, Chemistry, and Biology
Edited by Tobias Stauber
ISBN 978-1-119-46959-9

Volume 3: Graphene-Like 2D Materials
Edited by Mei Zhang
ISBN 978-1-119-46965-0

Volume 4: Composites
Edited by Cengiz Ozkan
ISBN 978-1-119-46968-1

Volume 5: Energy, Healthcare, and Environmental Applications
Edited by Cengiz Ozkan and Umit Ozkan
ISBN 978-1-119-46971-1

Volume 6: Biosensors and Advanced Sensors
Edited by Barbara Palys
ISBN 978-1-119-46974-2

Volume 7: Biomaterials
Edited by Sulaiman Wadi Harun
ISBN 978-1-119-46977-3

Volume 8: Technology and Innovation
Edited by Sulaiman Wadi Harun
ISBN 978-1-119-46980-3

Handbook of Graphene

Volume 3: Graphene-Like 2D Materials

Edited by
Mei Zhang
High-Performance Materials Institute,
Florida State University,
Tallahassee, Florida, USA

WILEY

This edition first published 2019 by John Wiley & Sons, Inc., 111 River Street, Hoboken, NJ 07030, USA and Scrivener Publishing LLC, 100 Cummings Center, Suite 541J, Beverly, MA 01915, USA

For more information about Scrivener publications please visit www.scrivenerpublishing.com.

Wiley Global Headquarters
111 River Street, Hoboken, NJ 07030, USA

For details of our global editorial offices, customer services, and more information about Wiley products visit us at www.wiley.com.

Library of Congress Cataloging-in-Publication Data

ISBN 978-1-119-46965-0

Cover image: Pixabay.Com
Cover design by Russell Richardson

Set in size of 11pt and Minion Pro by Manila Typesetting Company, Makati, Philippines

Printed in the USA

10 9 8 7 6 5 4 3 2 1

Contents

Preface

Despite being just a one-atom-thick sheet of carbon, graphene is one of the most valuable nanomaterials. Initially discovered through scotch-tape-based mechanical exfoliation, graphene can now be synthesized in bulk using various chemical techniques. Counted among the contrasting properties of this remarkable material are its lightweight, thinness, flexibility, transparency, strength, and resistance, along with superior electrical, thermal, mechanical, and optical properties. Due to these novel traits, graphene has attracted attention for use in cutting-edge applications in almost every area of technology, which are projected to change the world.

The *Handbook of Graphene* is presented in a unique eight-volume format covering all aspects relating to graphene—its development, synthesis, application techniques, and integration methods; its modification and functionalization; its characterization tools and related 2D materials; physical, chemical, and biological studies of graphene and related 2D materials; graphene composites; use of graphene in energy, healthcare, and environmental applications (electronics, photonics, spintronics, bioelectronics and optoelectronics, photovoltaics, energy storage, fuel cells and hydrogen storage, and graphene-based devices); its large-scale production and characterization; as well as graphene-related 2D material innovations and their commercialization.

This third volume of the handbook is solely focused on *Graphene-Like 2D Materials*. Some of the important topics include but are not limited to proximity-induced topological transition and strain-induced charge transfer in graphene/MoS2 bilayer heterostructures; planar graphene superlattices; magnetic and optical properties of graphene materials with porous defects; graphynes: advanced carbon materials with layered structure; nanoelectronic application of graphyne and its structural derivatives; twisted bilayer graphene: low-energy physics, electronic ,and optical properties; effects of charged coulomb impurities on low-lying energy spectra in graphene magnetic dot and ring; graphene in bioelectronics; graphene metamaterial electron optics: excitation processes and electro-optical modulation; linear carbon: from 1D carbyne to 2D hybrid sp–sp^2 nanostructures beyond graphene; band structure modifications in beyond graphene materials; chemically modified 2D materials: production and applications; black phosphorus saturable absorber for passive mode-locking pulses generation; and search for fundamental physics on table-top experiments with Dirac–Weyl materials.

In conclusion, thank you to all the authors whose expertise in their respective fields have contributed to this book as well as a sincere appreciation to the International Association of Advanced Materials.

February 15, 2019

1

Proximity-Induced Topological Transition and Strain-Induced Charge Transfer in Graphene/MoS_2 Bilayer Heterostructures

Sobhit Singh[1]*, Abdulrhman M. Alsharari[2], Sergio E. Ulloa[2] and Aldo H. Romero[1]

[1]Department of Physics and Astronomy, West Virginia University, Morgantown, West Virginia, USA
[2]Department of Physics and Astronomy, Nanoscale and Quantum Phenomena Institute, Ohio University, Athens, Ohio, USA

Abstract

Graphene/MoS_2 heterostructures are formed by combining the nanosheets of graphene and monolayer MoS_2. The electronic features of both constituent monolayers are rather well preserved in the resultant heterostructure due to the weak van der Waals interaction between the layers. However, the proximity of MoS_2 induces strong spin orbit coupling effect of strength ~1 meV in graphene, which is nearly three orders of magnitude larger than the intrinsic spin orbit coupling of pristine graphene. This opens a bandgap in graphene and further causes anti-crossings of the spin-nondegenerate bands near the Dirac point. Lattice incommensurate graphene/MoS_2 heterostructure exhibits interesting moiré patterns which have been observed in experiments. The electronic bandstructure of heterostructure is very sensitive to biaxial strain and interlayer twist. Although the Dirac cone of graphene remains intact and no charge-transfer between graphene and MoS_2 layers occurs at ambient conditions, a strain-induced charge-transfer can be realized in graphene/MoS_2 heterostructure. Application of a gate voltage reveals the occurrence of a topological phase transition in graphene/MoS_2 heterostructure. In this chapter, we discuss the crystal structure, interlayer effects, electronic structure, spin states, and effects due to strain and substrate proximity on the electronic properties of graphene/MoS_2 heterostructure. We further present an overview of the distinct topological quantum phases of graphene/MoS_2 heterostructure and review the recent advancements in this field.

Keywords: Heterostructure, graphene, transition metal dichalcogenide, charge transfer, Dirac point, tight binding model, topological phase transition, spin-orbit coupling, proximity effects, Berry curvature

1.1 Introduction

The successful isolation of graphene from bulk graphite [1] has triggered a new burgeoning research area in atomically thin two-dimensional (2D) materials. Since the last decade, several 2D materials namely – graphene, BN, MoS_2, $MoSe_2$, WS_2, WSe_2, $MoTe_2$, Xene sheets (X = Si, Ge, Sn), phosphorene, bismuthene, and many more, have been fabricated

**Corresponding author*: smsingh@mix.wvu.edu

Mei Zhang (ed.) Handbook of Graphene: Volume 3, (1–28) © 2019 Scrivener Publishing LLC

and extensively investigated due to their promising applications in the electronic, valleytronic, spintronic, catalysis, energy, and biosensing areas [2, 3, 4, 5, 6, 7, 8, 9, 10, 11, 12, 13]. Some of the notable properties that make 2D materials interesting are: high carrier mobility, superconductivity, mechanical flexibility, exceptional thermal conductivity, large photoluminescence, high optical and UV absorption, quantum spin Hall effect, strong light–matter interactions, and observation of highly confined plasmon–polaritons [2, 14, 15, 16]. Interestingly, these properties can be efficiently harnessed in 2D materials by means of strain engineering, number of atomic layers, adsorption, intercalation, interlayer twist, proximity effects, and gate voltage [17, 18, 19, 20]. Furthermore, several types of 2D materials can be vertically stacked to design van der Waals (vdW) heterostructures, which often enhance the desirable properties of the constituent atomic layers [17, 18, 19, 21]. These heterostructures offer unique ways to tailor their remarkable properties, hence they have promising applications in modern technology. However, control of the doping type, carrier concentration, and stoichiometry remains challenging in most of the known 2D materials and vdW heterostructures [21].

Graphene, a two dimensional monolayer of carbon atoms arranged in a honeycomb lattice, has emerged as the most celebrated 2D material of the last decade. It has been thoroughly investigated and many of its interesting features have been revealed [2]. A single layer graphene exhibits numerous novel features such as ultra-high intrinsic mobility (200,000 $cm^2/V^{-1}s^{-1}$), large electrical conductivity, excellent thermal conductivity (5,000 $W^{-1}K^{-1}$), biosensing, and exceptional elastic and mechanical properties with a very large Young's modulus (~1.0 TPa) [2, 22, 23]. However, the negligible intrinsic spin–orbit coupling (SOC) and correspondingly small energy bandgap limit many practical applications of pristine graphene in spintronics. In recent years, researchers have succeeded in enhancing the bandgap of graphene by several orders using unconventional methods and substrate proximity effects. The availability of many other 2D crystals allows us to design new graphene-based vdW heterostructures having strong proximity effects. A particular family of such 2D crystals is the semiconducting transition metal dichalcogenides (TMDs)-MX_2 (M = Mo, W and X = S, Se, Te) – that shows interesting optoelectronic and valleytronic features, and offer strong proximity effects on graphene's electronic bandstructure [24, 25, 26, 27, 28].

Atomically thin MX_2 semiconductors (M = W, Mo and X = S, Se, Te) form a sandwich structure with a honeycomb lattice [29], where one atomic layer of transition-metal atom (M) is sandwiched between two atomic layers of chalcogens (X). These semiconductors exhibit a strong SOC in their valence bands, which increases with increasing mass of the M atom. MoS_2 is one of the most widely studied TMDs with a tunable bandgap in the visible and infrared (IR) regions of the electromagnetic spectrum as the number of atomic layers in the crystal changes. Bulk MoS_2 exhibits an indirect bandgap of ~1.3 eV, which increases with decreasing number of layers [5, 30, 24, 25]. A monolayer of MoS_2 shows direct bandgap with energy gap of ~1.8 eV at K & K′ high symmetry points of the hexagonal Brillouin zone. Because of the broken inversion symmetry, SOC effects lift the spin-degeneracy of bands and substantially split the highest valence bands at the K & K′ points. This broken spin degeneracy, when combined with the time-reversal symmetry present in pristine MoS_2, yields inherently coupled electronic bands at K & K′ valleys, which results in the possible observation of spin-valley effects and optical polarization memory in these materials [15].

In pursuit of combining the novel features of graphene and MoS_2 monolayers, and mitigate their undesirable properties, researchers have recently made outstanding efforts to combine graphene and MoS_2 monolayers, and built graphene/MoS_2 vdW heterostructures [31, 32, 33, 18, 19]. Lattice incommensurate graphene/MoS_2 heterostructures show intriguing properties that can be controlled by tuning several factors such as strain, relative sliding between layers, interlayer twist, doping, bending, stacking order, and intercalation [34, 35, 36, 37, 38]. Due to the lattice mismatch between graphene and MoS_2 monolayer, moiré patterns are expected to appear in graphene/MoS_2 vdW heterostructures, which has been observed in the recent experiments [39, 26, 40].

The proximity of MoS_2 induces relatively strong SOC effects in graphene opening an energy bandgap at the Dirac point [41]. This bandgap can be further enhanced by means of gating and strain. Interestingly, the substrate induced SOC effects compete with the intrinsic SOC of graphene causing anti-crossing of spin–split bands near the Dirac point [28]. One can also realize distinct topological quantum phases in graphene/MoS_2 heterostructures by exploiting an interlink between the proximity effects, SOC, and the staggered potential [28]. In a recent work, Gmitra *et al.* [27] have demonstrated that a SOC induced band-inversion occurs near the Dirac point in graphene/WS_2 heterostructure, thanks to the large SOC of W, which yields a quantum spin-Hall phase with chiral edge states in the graphene/WS_2 heterostructure. A similar topological phase transition can be realized in graphene/MoS_2 heterostructures by applying a gate voltage [28]. In addition to these topological features, recent works report the observation of exceptional optical response with large quantum efficiency, gate-tunable persistent photoconductivity, excellent mechanical response, high power conversion efficiency, photocurrent generation, and negative compressibility in the graphene/MoS_2 heterostructures [31, 32, 33, 42, 43]. In regard to the practical applications, researchers have constructed electronic logic gates, transistors, memory devices, optical switches and biosensors using graphene/MoS_2 heterostructures [31, 32, 33, 42, 43, 37].

In this chapter, we review the structural, electronic and topological features of graphene/MoS_2 heterostructures. This chapter can be divided into two main parts: (i) Survey of results from the first-principles calculations, and (ii) Insights from the model Hamiltonian analysis and topological phase transitions. In the first part, we describe details regarding the crystal structure, interlayer effects, electronic bandstructure, nature of spin states and atomic orbitals near Fermi level, strain effects on the electronic bandstructure, and charge-transfer phenomena. In the second part, we investigate the proximity effects and generic features of graphene/MoS_2 heterostructures using a tight binding formalism to obtain parameters for the symmetry-allowed low-energy effective Hamiltonian. Effects of the gate voltage on the dynamics of the bandstructure are discussed. Calculations of Berry curvature and Chern number confirm the occurrence of topological phase transitions at a critical gate voltage. The details of Density Functional Theory (DFT) calculations are given in the Appendix.

1.2 Results from the DFT Calculations

1.2.1 Insights into the Graphene/MoS_2 Heterostructure

The optimized crystal structure of graphene/MoS_2 bilayer heterostructure is given in Figure 1.1a–b. Large lattice mismatch between graphene and MoS_2 monolayers makes the

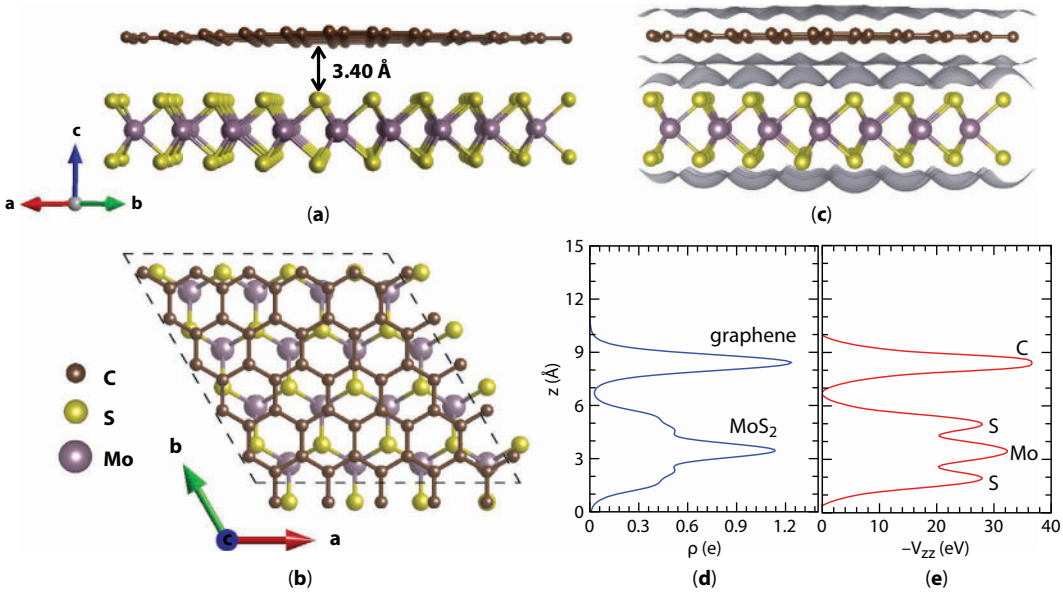

Figure 1.1 (Color online) Figures (a–b) show the crystal structure of 5:4 graphene/MoS_2 bilayer heterostructure from two different perspectives. (c) Isodensity charge surfaces (gray color) at isosurface value 0.007 for 5:4 graphene/MoS_2 bilayer heterostructure. The planar average of (d) charge density (ρ) and (e) electrostatic potential (V_{ZZ}) along the vertical ***Z*** direction. Notice the negative sign of V_{ZZ} in Figure (e).

ab initio modeling of graphene/MoS_2 heterostructure computationally demanding. In order to minimize the lattice mismatch, one can vertically stack two commensurate supercells of graphene and monolayer MoS_2. The two most commonly used graphene/MoS_2 heterostructures are: (i) $(4 \times 4)/(3 \times 3)$ (hereafter 4:3), and (ii) $(5 \times 5)/(4 \times 4)$ (hereafter 5:4), where the latter has relatively smaller lattice mismatch but larger number of atoms/cell. In graphene/MoS_2 heterostructures, graphene and MoS_2 monolayers weakly interact through long-range vdW interactions. The experimentally reported interlayer distance between graphene and MoS_2 nanosheets is 3.40 ± 0.1 Å [44]. However, numerous first-principles studies inconsistently predicted interlayer gap values ranging from 3.1 Å to 4.3 Å [27, 34, 45–51]. This is mainly because of the inadequate evaluation of weak non-local vdW interactions within the DFT framework. Although, various DFT-vdW methods [50–52] have been employed and found to be inadequate in describing this system, it has been reported that the Tkatchenko–Scheffler (TS) method [53] for vdW corrections efficiently evaluates the long-range vdW interactions in this system, and accurately predicts the interlayer spacing (3.40 Å) between graphene and MoS_2 nanosheets [54], which is in remarkable agreement with the experimental data. The main reason behind the success of the TS method is the fact that it accounts for the non-local charge density fluctuations near the interface, whereas most of the other DFT-vdW methods are insensitive to the chemical environment. Therefore, it is expected that compared to other DFT-vdW methods, the TS method might perform better in evaluating the weak vdW interaction between a metallic and an insulating material interface, where fluctuations in charge density are very large [54].

The optimized lattice parameters of the 5:4 bilayer with minimal lattice mismatch are $a = b = 12.443$ Å [54]. The Mo-S and C-C bond lengths are 2.38 and 1.44 Å, respectively. In this

case, the MoS_2 monolayer is being compressed by 0.3%, whereas the graphene monolayer is being stretched by 1.16% from the pristine case. The vertical distance between S-S atomic planes, *i.e.* the absolute thickness of the MoS_2 monolayer is 3.13 Å. Figure 1.1c shows the charge density isosurface near the interface. One can notice a small charge overlap between two constituent monolayers. This charge overlap is originating due to the weak vdW effects, and it could cause enhancement in the direct bandgap at Dirac point, as predicted by McCann [55]. Variation in the planar average of charge density (ρ) and planar average of total local potential (V_{zz}) along the vertical z direction is shown in Figure 1.1d–e. Here, V_{zz} only includes the electrostatic part of potential without inclusion of the exchange-correlation term. Notably, there exists a potential difference between graphene and MoS_2 monolayers indicating presence of a non-zero dipole moment pointing towards the graphene layer. The amplitude of this dipole moment is ~0.62 Debye in graphene/MoX_2 and ~0.66 Debye in graphene/WX_2 heterostructures (X = S, Se) [56].

1.2.2 Electronic Bandstructure: Orbital and Spin Configurations

Figure 1.2 shows the electronic bandstructure of two graphene/MoS_2 heterostructures (5:4 and 4:3) calculated with vdW + SOC along the high symmetry directions of the hexagonal Brillouin zone. The electronic features of graphene and MoS_2 monolayers are well preserved due to the weak vdW interaction between the monolayers. The linear dispersion of the Dirac cone lies within the bandgap of the MoS_2 monolayer in the 5:4 bilayer heterostructure. Contribution of various atomic orbitals to the electronic bands is shown in Figure 1.2c–d. Knowledge of the atomic orbitals near the Fermi level is crucial for many theoretical and experimental investigations, such as: tight-binding calculations, determination of optical properties, charge carrier dynamics, photocatalysis, etc. Here, two notable features are: (i) the conduction and valence band of MoS_2 near the Fermi level are mainly composed of Mo-d_{z^2}, d_{xy} and $d_{x^2-y^2}$ orbitals, and (ii) the Dirac cone is formed by the π bonded C-p_z orbitals situated at A and B sublattices of graphene. The lowest conduction band near the Dirac point arises from the p_z orbitals at the A-site, while the highest valence band arises from the p_z orbitals at the B-site. All other states contribute to bands far from the Fermi level as shown in Figure 1.2c–d [54].

The weak vdW interaction between graphene and MoS_2 monolayers yields a small, yet significant, bandgap at the Dirac point. The bandgap in 5:4 bilayer is ~0.4 meV which increases almost by three times in 4:3 bilayer heterostructure due to the relatively larger lattice mismatch present in the 4:3 bilayer. Another interesting feature we observe in 4:3 bilayer heterostructure is the shift of the optical (direct) bandgap of MoS_2 monolayer from K to the Γ point of Brillouin zone. In a 5:4 bilayer heterostructure, the MoS_2 monolayer preserves its direct bandgap semiconducting nature at the K-point with a direct bandgap of ~1.8 eV, which is in excellent agreement with the reported values in the literature [57–60]. However in a 4:3 bilayer, the lowest conduction band shifts lower in energy at the Γ-point, whereas the highest valence band (at Γ-point) shifts higher in energy than the valence band maximum at the K-point. These two bands have Mo-d_{z^2} character at Γ-point. Consequently, the direct energy gap of MoS_2 monolayer decreases in magnitude and shifts from the K-point to the Γ point of Brillouin zone. Since the 5:4 graphene/MoS_2 bilayer heterostructure maintains the

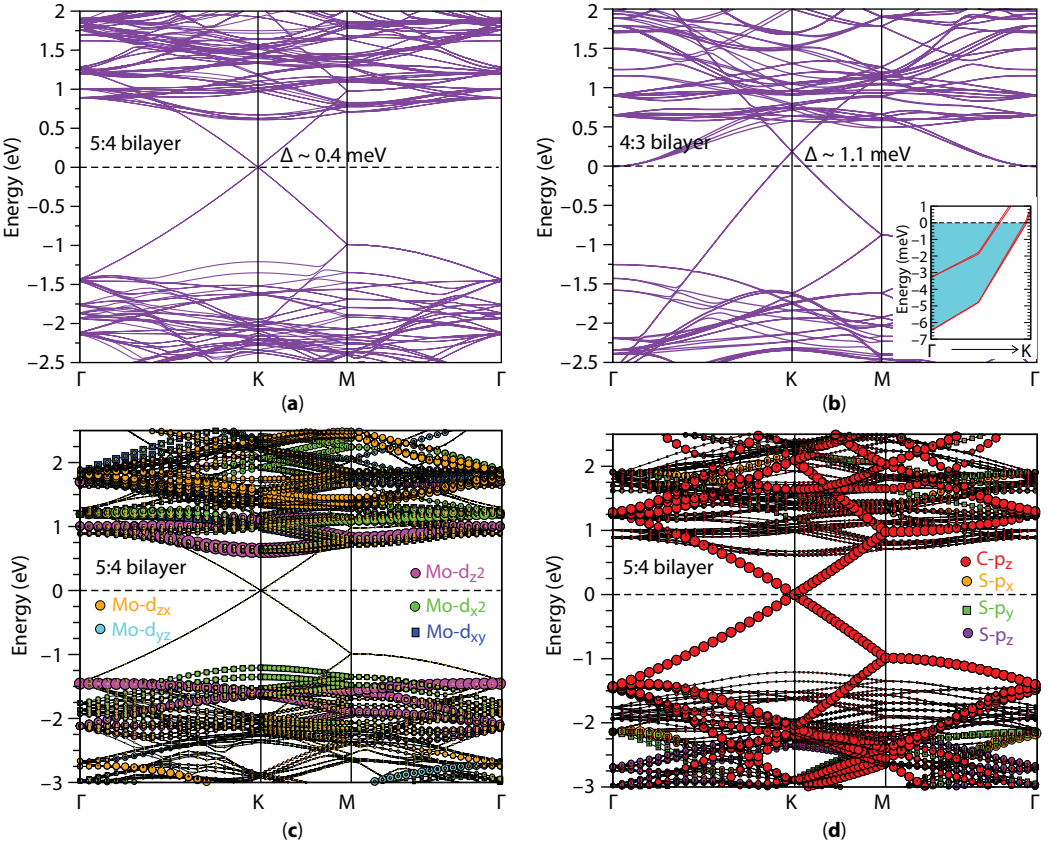

Figure 1.2 (Color online) The electronic bandstructures of (a) 5:4, and (b) 4:3 bilayer heterostructures calculated with vdW + SOC. Inset of Figure (b) shows an enlarged view of the conduction bands near the Γ point. Figures (c–d) represent the projection of atomic orbitals on the electronic bands of 5:4 bilayer. Horizontal dotted line at 0.0 eV energy marks the Fermi level.

direct gap nature of MoS_2 monolayer at the K-point, it can be concluded that the aforementioned transition in 4:3 bilayer is primarily triggered by the strain effects arising due to the large lattice mismatch [54].

Signatures of charge-transfer between the graphene and MoS_2 layers can be observed in Figure 1.2b. The Dirac point in 4:3 bilayer is shifted above the Fermi level and resides above the lowest conduction band with MoS_2 character. This indicates transfer of electrons from graphene to MoS_2 monolayer. This charge-transfer process can be harnessed by means of bi-axial strain or gate voltage, and is of central interest for technological applications [61, 31]. The netshift of Dirac point above the Fermi level is ~ 0.18 eV. Since the Dirac point has shifted above the Fermi level, the bottom of the conduction band of MoS_2 is expected to dip below the Fermi level to catch the electrons transferred from graphene. In fact, a careful investigation of the lowest conduction band of MoS_2 near the Fermi level shows that the Fermi level is almost 6.5 meV above the bottom of the conduction band at the Γ-point, thus suggesting the presence of an electron pocket at the Γ-point [see the inset of Figure 1.2b].

No such charge-transfer has been observed in 5:4 bilayer heterostructure which has minimal strain. This finding is consistent with the experimental observations of Diaz *et al.* [62]. In 2015, Diaz *et al.* performed angle-resolved photoemission spectroscopic (ARPES) measurements to probe the electronic structure of graphene/MoS_2 heterostructure. They observed that the Dirac cone of graphene remains intact and no significant charge-transfer occurs between the graphene and MoS_2 layers. However, bandgaps are reported away from the Dirac point due to the proximity of MoS_2 [62].

After discussing the nature of orbitals and energy bandgap, we focus our attention on the spin related features of the electronic states in the graphene/MoS_2 bilayer. Figure 1.3 shows the projection of S_x, S_y, and S_z components of spin on the electronic bandstructure of the 5:4 bilayer. Similar spin features are present for the 4:3 bilayer. The spin quantization axis was chosen along the (001) direction. As one can notice in Figure 1.3, the S_z component of spin plays the dominant role in governing the spin features of bands near the Fermi level, while the contribution of S_x and S_y projections is negligible. In the top panels of Figure 1.3, we plot the spin projection on selected graphene and MoS_2 bands near Fermi level, whereas the bottom panels show an enlarged view close to the neutrality point. In Figure 1.3a, one can observe that Mo-*d* top valence bands spin-split near the K-point due to the broken inversion symmetry (marked by red and blue arrows). The spin-splitting (Δ_{VB}) is ~0.2 eV at the K-point, which is not significantly affected by the nearby graphene layer. Notice this is much smaller than that reported for WX_2 monolayers

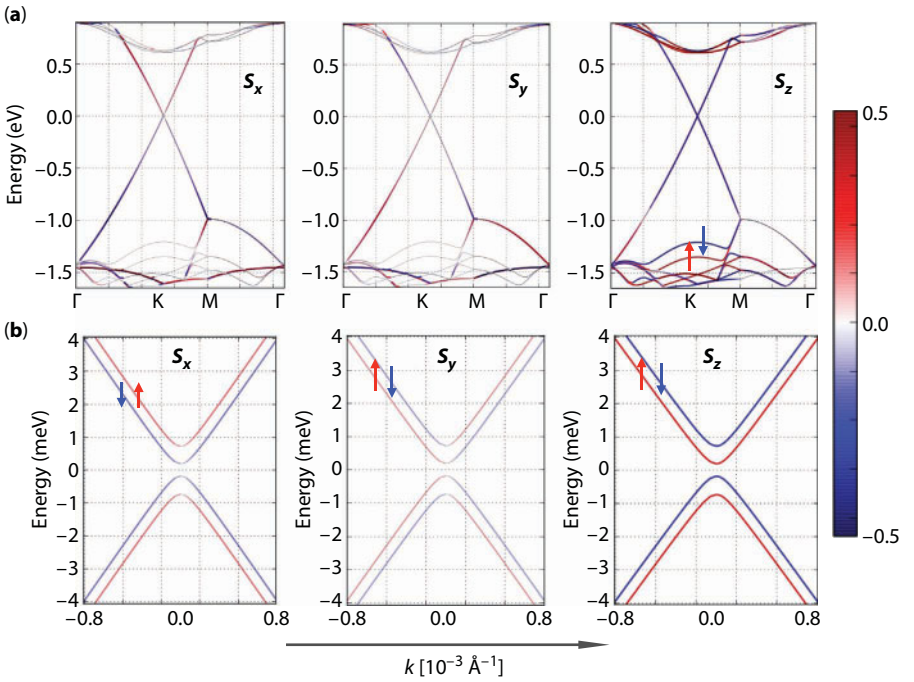

Figure 1.3 (Color online) Projection of S_x, S_y, and S_z components of spin on the electronic bandstructure of the 5:4 bilayer heterostructure. Figures in the top panels (a) show various spin contributions on the selected bands near the Fermi level. Figures in the bottom panels (b) show the enlarged view of spin-splitting in bands near the Dirac point. The ***k***-path in lower panels is centered at the hexagonal Brillouin zone K-point. Red (Blue) color depicts spin up (down) states.

(X = S, Se, Te). The value of Δ_{VB} for WS_2, WSe_2, and WTe_2 is 0.43 eV, 0.47 eV, and 0.48 eV, respectively [63, 64]. This is as expected from the difference in the atomic numbers of S, Se, and Te.

An enlarged view of bands near the Fermi energy reveals that bands acquire a parabolic shape near the Dirac point due to proximity effects. A Rashba-type spin-splitting is expected in this system because of the broken inversion symmetry and strong SOC effects arising from the MoS_2 layer. Moreover, due to the intrinsic SOC of graphene, a spin-gap opens at the Dirac point and bands anti-cross each other yielding the resulting band dispersion shown in Figure 1.3b [54]. Staggered potential effects further enhance the bandgap opening. By harnessing the aforementioned competitive terms, one can realize distinct topological phases in this bilayer system [28]. A controlled phase transition between the distinct topological phases can be achieved either by tuning strength of SOC from the TMDC layer or by applying a relative gate voltage between the layers [28]. We discuss this issue in more detail later using a model Hamiltonian.

1.2.3 Strain Effects and Charge Transfer

As we mentioned above while discussing the electronic bandstructure of 5:4 and 4:3 bilayer heterostructures, the shifting of the Dirac point above the lowest conduction band of MoS_2 indicates the occurrence of a charge-transfer from graphene to the MoS_2 monolayer. We also argued that this charge-transfer is mainly triggered by strain. The effect of strain on the electronic properties of graphene [65, 66, 67, 68, 69, 70, 71, 72] and MoS_2 [73, 74, 75, 76, 77, 78, 79, 80, 81, 30, 82, 83] has been well evaluated in the literature from both theoretical and experimental studies. These studies conclude that the electronic properties of both graphene and MoS_2 monolayer can be considerably harnessed by strain engineering and novel features can be realized in these monolayer systems. At moderate strains, graphene maintains its semimetallic feature. No significant changes in the electronic bandstructure of graphene have been observed for strains up to ~15%. However, depending upon the magnitude and direction of applied strain, Dirac cone can be shifted away from the K point. Choi *et al.* [69] predicted that no sizable energy gap opens in the uniaxially strained graphene under uniaxial strain less than 26% along any arbitrary direction. They further suggested that the low-energy dispersion of bands in moderately uniaxially strained graphene can be modeled using the generalized Weyl's equation [69]. As the uniaxial strain increases, the Fermi velocity of Dirac cone varies (increases or decreases) depending upon the direction of the wave vector [69]. Interestingly, Guinea *et al.* [70] have reported that a designed strain aligned along three main crystallographic directions could induce strong gauge fields, which effectively act as a uniform pseudomagnetic field.

On the other hand, at a critical value of strain, the valence band maxima of MoS_2 at Γ increases in energy, shifting towards the Fermi level, and supersedes the valence band maxima of MoS_2 at K, thus resulting in a direct to indirect bandgap transition in the strained monolayer. A number of theoretical as well as experimental studies have concluded that this bandgap transition occurs in MoS_2 at 0.5–1.0% compressive or tensile strain [73, 74, 75, 76, 77, 78, 79, 80, 81, 30, 82, 83]. Considering many-body and SOC effects, Wang *et al.* [84] predicted that the direct to indirect gap transition in MoS_2 monolayer should occur at 2.7% strain [82]. Under a tensile strain, the thickness of the MoS_2 monolayer (*i.e.* separation between S-S planes) decreases owing to its positive Poisson's ratio [85], which results in enhanced hybridization of S-p_z orbitals that contribute to the valence band maxima at Γ.

However, Mo-d_{z^2} orbitals mostly remain unaltered under the biaxial strain conditions, while Mo-d_{xy} and Mo-$d_{x^2-y^2}$ states suffer energy shifts when strain is imposed. Such strain-induced direct to indirect bandgap transition manifests as decreasing photoluminescence intensity of MoS_2 monolayer and it can be clearly traced in experiments [77]. The energy bandgap of MoS_2 decreases upon application of strain. Moreover, the effective mass of electrons and holes at K and Γ points decreases with increasing strain [82, 84]. The rate of reduction for hole effective mass at Γ is much higher compared to the reduction of electron effective mass at K. For instance, the effective mass for holes is reduced by more than 60% at Γ, while the effective mass of electrons at K drops by 25% for a tensile strain of 5% [82]. Interestingly, a semiconductor to metal transition is predicted in MoS_2 monolayer at a tensile strain of ~10% and at a compressive strain of ~15% [82].

Notably, the direct to indirect bandgap transition in MoS_2 can also be achieved by vertically stacking two or more monolayers. With increasing number of layers, the interaction between the Mo-d_{z^2} orbitals of different S-Mo-S nanosheets increases which leads to an upshift of the energy bands. Consequently, the valence band maximum at Γ and conduction band minimum at K shift towards higher energy values, whereas other states do not change much being mainly composed of *d* orbitals lying in $x - y$ plane. For this reason, multilayer MoS_2 exhibits an indirect bandgap between the valence band maximum at Γ and the conduction band minimum along the Γ – *K* path [82].

In the simplest approximation, it can be assumed that Mo atoms primarily suffer the interfacial strains caused by the substrate, whereas S atoms relax according to the modified location of the strained Mo atoms. Here, we perform a computational exercise to understand the effect of biaxial strain on Mo atoms on the electronic structure of graphene/MoS_2 heterostructure. We apply biaxial strain on Mo atoms in the well optimized 5:4 graphene/MoS_2 bilayer heterostructure and fully relax the S atoms in the strained cell. Biaxial strain (x) ranging from –4% (compressive strain) to +4% (expansion or tensile strain) was employed on Mo atoms. This computational exercise roughly models the local substrate induced strain effects on the Mo atoms which disrupt the ordering of Mo atoms in lattice yielding formation of domains or grain boundaries at finite intervals. In our case, grain boundaries would be formed at the edge of the unit cell of dimensions: $a = b = 12.44$ Å, where two Mo atoms from adjacent periodic cells would either come close to each other or move away depending upon the tensile or compressive strains employed on the Mo atoms, respectively. Figure 1.4

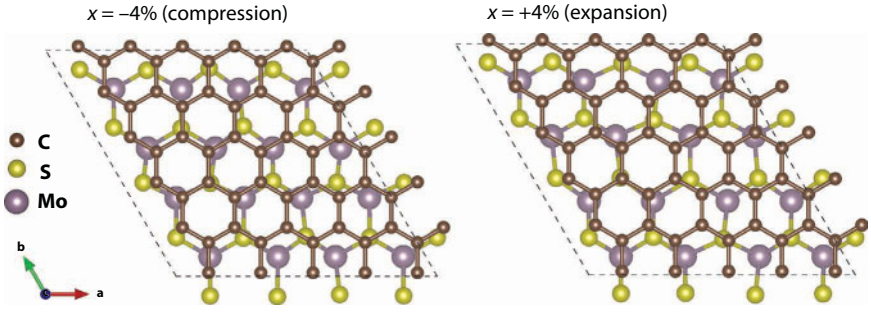

Figure 1.4 (Color online) Figures show the crystal structure of biaxially strained 5:4 graphene/MoS_2 bilayer from the top view. Left panel represents the case when Mo atoms are compressed by 4% (*i.e.* $x = -4\%$) while right panel represents the case when Mo atoms are expanded by +4% (*i.e.* $x = +4\%$).

shows the crystal structure of strained 5:4 graphene/MoS_2 bilayer heterostructure for two extreme cases of employed biaxial strain (x) on Mo atoms. Positive/Negative values indicate the tensile/compressive strain. We observe a small increase in the absolute thickness of MoS_2 monolayer with increasing compressive strain which is as expected due to the positive Poisson's ratio of MoS_2 monolayer [85]. Because of the weak vdW interaction between graphene and MoS_2 nanosheets, we notice a negligible change in the interlayer separation with varying x, which is consistent with changing MoS_2 thickness. The maximum change in interlayer distance is ±0.02 Å at the extreme values of imposed strains on Mo atoms.

Figure 1.5 shows the electronic bandstructure of 5:4 graphene/MoS_2 bilayer having strained Mo atoms. Both compressive and tensile strains yield similar features in the electronic bands. With increasing strain on Mo atoms, both valence and conduction Mo-d bands shift towards the Fermi level decreasing the net bandgap of the MoS_2 monolayer. However, MoS_2 maintains the direct bandgap nature in the studied range of strain. This finding is important since it suggests that graphene/MoS_2 heterostructure mounted on a suitable substrate that imposes small interfacial strain on Mo atoms can be considerably tuned by controlling the substrate-imposed strain on Mo atoms. This effect can be present in photoluminescence experiments [86, 87]. One can also notice that the effective mass of charge carriers in MoS_2 monolayer increases with increasing strain on Mo atoms.

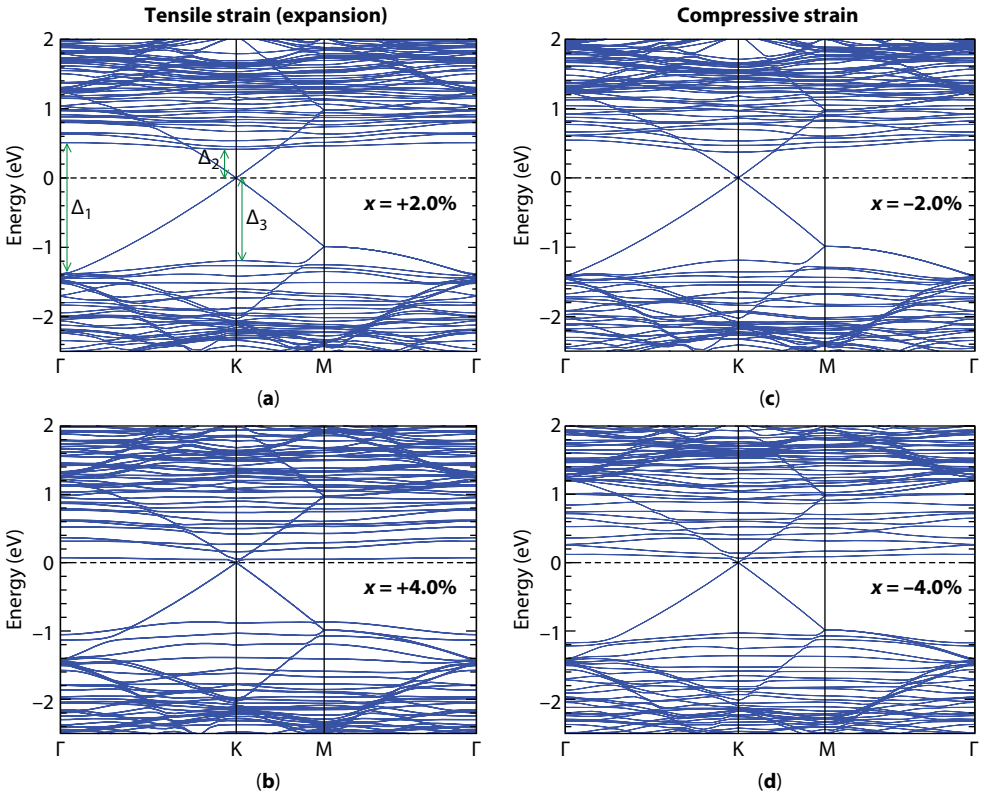

Figure 1.5 (Color online) Figures show the electronic bandstructure of strained Mo atoms in 5:4 graphene/MoS_2 bilayer heterostructure calculated without SOC. Figures (a) and (b) represent bands for 2.0% and 4.0% tensile strains, whereas Figures (c) and (d) represent bands for 2.0% and 4.0% compressive strains, respectively.

In order to further understand the effect of strain on the direct bandgap at Dirac point, location of band edges of MoS_2 monolayer, and change in the orbital features near the Fermi level, we plot the aforementioned quantities as a function of x in Figure 1.6. Projection of various atomic orbitals on the electronic bands for $x = -4\%$ case reveals the nature of orbitals near the Fermi level is preserved in the studied range of imposed strain on Mo atoms. The direct bandgap at Dirac point increases substantially with increasing strain on Mo atoms [see Figure 1.6a]. This can be attributed to the enhanced hybridization between d_z and p_z orbitals. Figure 1.6b shows variation in Δ_1, Δ_2, and Δ_3 versus x. Here, Δ_1 represents the energy difference between the lowest conduction and highest valence bands at Γ, Δ_2 refers to the energy difference between the lowest conduction band of Mo-d states and Dirac point, and Δ_3 represents that between the Dirac point and the highest valence band of Mo-d states [see Figure 1.5a for illustration]. Our analysis shows Δ_1, Δ_2, and Δ_3 decreasing with increasing strain on Mo atoms. With increasing x, the Dirac point comes closer to the conduction bands of MoS_2, and at $x = \pm 4\%$ the lowest conduction band of Mo-d states

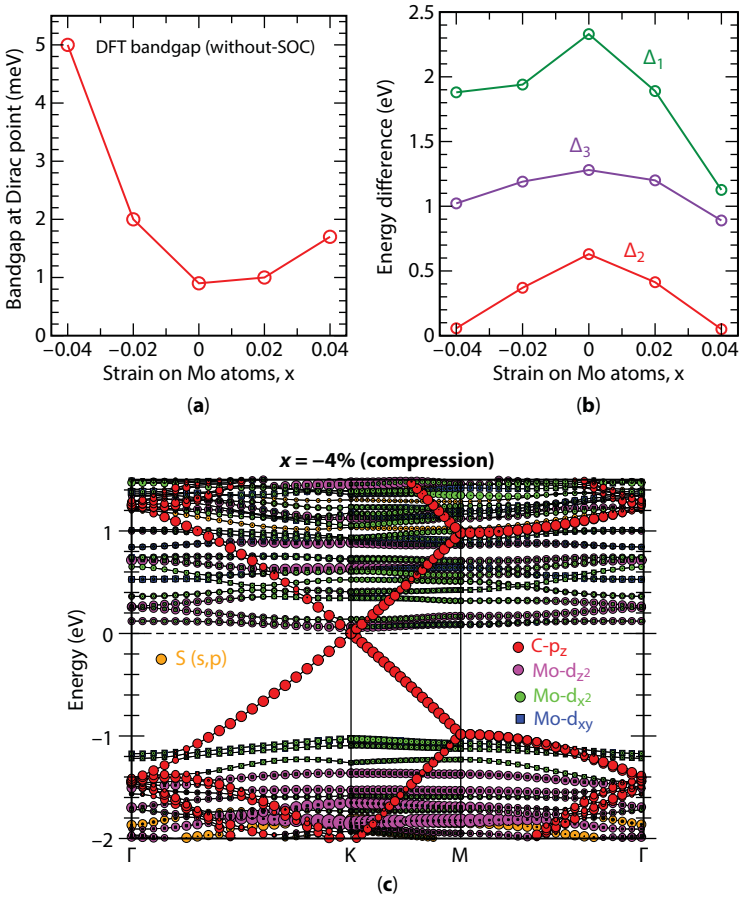

Figure 1.6 (Color online) Figures (a) and (b) represent change in the direct bandgap at Dirac point, and quantities Δ_1, Δ_2, and Δ_3 as a function of the strain on Mo atoms – x. See Figure 1.5a for definition of Δ_1, Δ_2, and Δ_3. (c) Projection of the selected atomic orbitals on the electronic bands of 5:4 graphene/MoS_2 bilayer heterostructure having 4% compressively strained Mo atoms. This bandstructure was calculated without inclusion of SOC.

almost touches the Dirac point. Therefore, beyond $x = \pm 4\%$ strain, a charge-transfer may occur from graphene to MoS_2 monolayer.

From the above discussion, it can be concluded that by tuning the substrate-induced strain on Mo atoms, one can harness the optical properties of graphene/MoS_2 bilayer heterostructure and further control the charge-transfer process between the two monolayers. From an experimental perspective, this can be achieved by choosing a suitable piezoelectric or flexoelectric substrate.

1.3 Model Hamiltonian and Topological Phase Transitions

1.3.1 Basic Theoretical Model

In this section, we study the heterostructure using a tight-binding theoretical framework. First, a linear transformation that connects the primitive lattice vectors of graphene and MoS_2 is written as [88],

$$\begin{pmatrix} \mathbf{a}_{G_1} \\ \mathbf{a}_{G_2} \end{pmatrix} = M \cdot \begin{pmatrix} \mathbf{a}_{\mathrm{M}_1} \\ \mathbf{a}_{\mathrm{M}_2} \end{pmatrix}, \tag{1.1}$$

where $\mathbf{a}_{x_1} = a_x\left(\frac{\sqrt{3}}{2}, \frac{1}{2}\right)$ and $\mathbf{a}_{x_2} = a_x\left(\frac{\sqrt{3}}{2}, \frac{-1}{2}\right)$ are the real primitive vectors (for x = graphene and MoS_2) with $M = diag\left(\frac{4}{5}, \frac{4}{5}\right)$. It can be shown [88] that the resulting moiré pattern has primitive lattice vectors ($\mathbf{R}_1$ and $\mathbf{R}_2$) given by

$$\begin{pmatrix} \mathbf{R}_1 \\ \mathbf{R}_2 \end{pmatrix} = [1 - M]^{-1} M \cdot \begin{pmatrix} \mathbf{a}_{\mathrm{M}_1} \\ \mathbf{a}_{\mathrm{M}_2} \end{pmatrix} \tag{1.2}$$

Because of the honeycomb structure, the Brillouin zone of the graphene/MoS_2 4:5 heterostructure has similar features to graphene, with two valleys $\mathbf{K}' = \frac{2\pi}{a_\alpha}\left(\frac{1}{\sqrt{3}}, \frac{-1}{3}\right)$, $\mathbf{K} = \frac{2\pi}{a_\alpha}\left(\frac{1}{\sqrt{3}}, \frac{1}{3}\right)$, $a_\alpha = 5a_G = 4a_M$, where the K and K′ valleys of graphene and MoS_2 are mapped onto the same positions of the first Brillouin zone of the supercell upon folding [see Figure 1.7c].

We use a tight-binding formalism that couples up to next nearest neighbors ≪ij≫ in MoS_2 with minimal three-orbital basis. In MoS_2, the basis can be represented at low energy by three orbitals (d_{z^2}, d_{xy} and $d_{x^2-y^2}$), as discussed above and in Ref. [89], so that

$$\mathrm{H}_M = \sum_{i,\sigma,\nu} \varepsilon_{\nu,\sigma} \alpha^\dagger_{i\nu\sigma} \alpha_{i\nu\sigma} + \sum_{\langle\langle ij \rangle\rangle,\nu\mu,\sigma} t_{i\nu,j\mu} \alpha^\dagger_{i\nu\sigma} \alpha_{j\mu\sigma} + h.c., \tag{1.3}$$

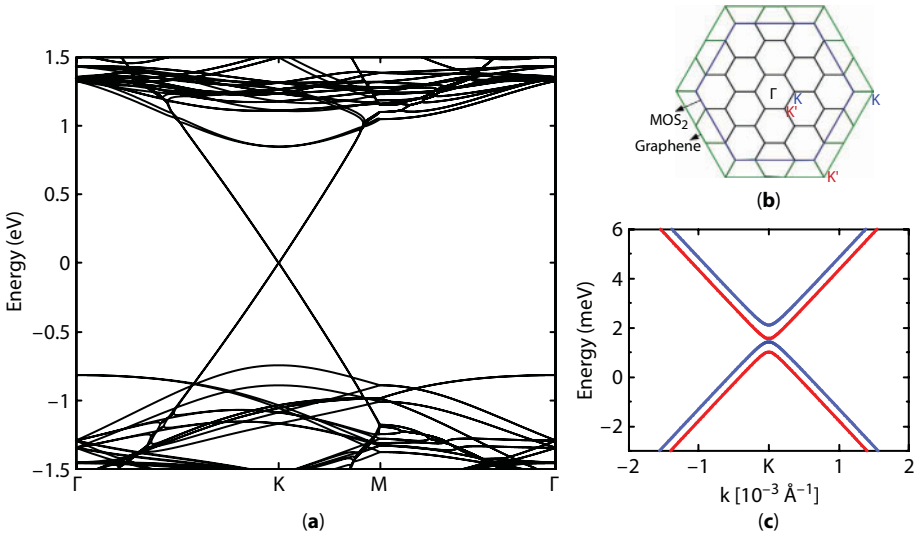

Figure 1.7 (Color online) Graphene/MoS_2 heterostructure in tight-binding description. (a) Band dispersion of graphene/MoS_2 along high symmetry lines Γ-K-M-Γ. (b) Brillouin zones of the reciprocal lattices. (c) Zooming near K valley shows that graphene bands are gapped and spin polarized due to the proximity of MoS_2. Blue (red) bands represent spin down (up) states. A graphene and MoS_2 monolayer first Brillouin zones (BZ) are shown as green and blue hexagon, respectively. Their relative K and K' valleys are also shown. The supercell BZ has a smaller reciprocal lattice size which upon folding, maps corner valleys from both layers onto the same point [28]. Compare this figure with Figure 1.2, showing similar features, although here the Fermi level is symmetric in the TMD gap.

where $\alpha^{\dagger}_{j\nu\sigma}$ label the ν-orbital at site j of the Mo-lattice with spin σ. The first term considers the on-site energy of atom j and orbital ν. The second term describes hopping between Mo orbitals to nearest and next nearest neighbors. Strong MoS_2 spin orbit coupling is considered from the atomic SOC contribution, (see Eq. 25 and Table IV in Ref. [89]).

To model graphene, we adopt the usual single-orbital representation for the triangular lattice with two-atom basis that couples only nearest neighbors <ij> [2],

$$\mathrm{H}_G = \sum_{i,\sigma} \varepsilon_{i,\sigma} c^{\dagger}_{i\sigma} c_{i\sigma} - t_g \sum_{<ij>,\sigma} (c^{\dagger}_{i\sigma} c_{j\sigma} + h.c.), \tag{1.4}$$

where ε of the first term describes the on-site energy, and the second term considers hoppings to the nearest neighbors with coupling strength t_g.

The presence of a substrate generates a perpendicular electric field to the graphene layer. This electric field causes a spin orbit coupling that can be described by a Rashba Hamiltonian of the form [90]

$$\mathrm{H}_R = it_R \sum_{\langle ij\rangle;\alpha,\beta} \hat{e} \cdot \left(\boldsymbol{s}_{\alpha\beta} \times \boldsymbol{d}^{\circ}_{\boldsymbol{ij}} \right) c^{\dagger}_{i\alpha} c_{j\beta}, \tag{1.5}$$

where α,β describes spin up and spin down states, $d_{ij}^{\circ} = \frac{d_{ij}}{|d_{ij}|}$ is the unit vector that connects A atom of graphene to its nearest neighbor B atom. The Rashba spin orbit interaction is weak in graphene, i.e. t_R = 0.067 meV [91]. This captures the mirror symmetry breaking effect. As a consequence, the spin is no longer a good quantum number and spin states interact with each other, opening anti-crossings at degeneracy points.

We consider coupling only between neighbors across the layers between the graphene p_z-orbital and MoS_2 d-orbitals, which is described as

$$\mathrm{H} = \sum_{<ij>,\nu\sigma} t_{i,j}^{\nu} c_{i\sigma}^{\dagger} \alpha_{j\nu\sigma} + h.c. \tag{1.6}$$

where $t_{i,j}^{\nu}$ is represented by a tunneling amplitude

$$t_{i,j}^{\nu} = t_{\nu} \exp\left[-|\mathbf{r}_{m,i} - \mathbf{r}_{g,j}|/\eta\right], \tag{1.7}$$

where $|\mathbf{r}_{m,i} - \mathbf{r}_{g,j}|$ is the distance that connects atoms in both layers, normalized to a constant $\eta = 5a_g$. t_{ν} describes the effective coupling between p_z and d-orbitals using a Slater–Koster approach [92]. It takes the form [28]

$$\begin{aligned}
t^{z^2} &= \left\langle p_z|H|d_{z^2}\right\rangle \\
&= -\sqrt{3}n_z^3 V_{pd\pi} - \frac{1}{2}n_z(n_x^2 + n_y^2 - 2n_z^2)V_{pd\sigma} \\
t^{x^2-y^2} &= \left\langle p_z|H|d_{x^2-y^2}\right\rangle \\
&= \frac{\sqrt{3}}{2}(n_z n_x^2 n_y^2)V_{pd\sigma} - (n_z n_x^2 n_y^2)V_{pd\pi} \\
t^{xy} &= \left\langle p_z|H|d_{xy}\right\rangle \\
&= n_x n_y n_z(\sqrt{3}V_{pd\sigma} - 2V_{pd\pi}),
\end{aligned} \tag{1.8}$$

where n_i are directional cosines. The numerical values of the coupling constants are set to be in agreement with what is expected: the coupling t^{z^2} is larger than t^{xy} and $t^{x^2-y^2}$, due to a higher overlap. The numerical values used here, $V_{pd\pi}$ = –0.232 eV and $V_{pd\sigma}$ = 0.058 eV, do not affect the main conclusions nor qualitative behavior, as we will discuss below. This Hamiltonian is capable of reproducing the low energy dispersions close to the K and K′ points with great accuracy. TMD parameters are adapted from Liu *et al.* [89], while for graphene we take the on-site energy to be zero and hopping parameter t_g = 3.03 eV [2].